Published in Sensors and Actuators B: Chemical 123, issue 1, 636-646, 2007
which should be used for any reference to this work

Magnetohydrodynamic pumping in nuclear magnetic resonance environments

A. Homsy *, V. Linder, F. Lucklum [1], N.F. de Rooij

University of Neuchatel, Institute of Microtechnology, SAMLAB, Rue Jaquet-Droz 1, CH-2002 Neuchatel, Switzerland

Abstract

We present a DC magnetohydrodynamic (MHD) pump as component of a nuclear magnetic resonance (NMR) microfluidic chip. This is the first time that MHD pumping in an NMR environment was observed and demonstrated. This chip generates a maximum flow rate of 1.5 μL min^{-1} (2.8 mm s^{-1} in the microchannel) for an applied voltage of 19 V with only 38 mW of power consumption in a 7 T superconductive magnet. We developed a simple method of flow rate measurement inside the bulky NMR magnet by monitoring the displacement of a liquid–liquid interface of two immiscible liquids in an off-chip capillary. We compared and validated this flow measurement technique with another established technique for microfluidics based on the displacement of microbeads. This allowed us to characterize and compare the flow rate generated by the micropump on top of a permanent magnet ($B_1 = 0.33$ T) with the superconductive magnet ($B_0 = 7.05$ T). We observed a 21-fold increase in flow rate corresponding to the ratio of the magnetic field intensities ($B_0/B_1 = 21$) in accordance with the theoretical flow dependence on the magnetic field intensity. The final aim is to integrate MHD pumps together with planar coils in a microfluidic system for NMR analysis. The high performance of MHD pumps at relatively low flow rates is seen as an asset for NMR and MRI applications.

Keywords: Magnetohydrodynamic flow; DC MHD; Micropump; NMR analysis

1. Introduction

Precise control of small volumes of sample is of great interest in microfluidics and for developing portable, micro total analysis systems (μTAS). More specifically, low and precise flow rates are imperative for the manipulation of fluids within an on-chip NMR system. Nuclear magnetic resonance is one of the most powerful chemical analysis techniques that takes place in high static magnetic field environments (B_0). In this paper, we present a microfluidics-based micropump using magnetohydrodynamics (MHD) for the manipulation of fluids in an NMR environment. Magnetohydrodynamic micropumps operate without moving parts, require only low voltages (less than 10 V) for their actuation, and the flow generated is continuous. Furthermore, MHD allows pumping of biological samples with high ionic strength, and liquid flow does not depend on the chemical nature of the capillary surface unlike in electro-osmotic flow. Forward and reverse flows are possible, with a flow profile similar to that observed for pressure-driven flows. For all these reasons, MHD pumping has attracted a growing interest for the handling of conductive fluids in microchannels over the past few years.

One of the first demonstrations of MHD pumping of saline solutions (seawater) in microchannels was presented by Jang and Lee [1]. The microchannels, made in silicon, were closed, the applied current was DC and MHD pumping was induced using a permanent DC magnet. The observed maximum flow rate was 63 μL min^{-1}. However, electrolysis of water led to the formation of gas bubbles in the channel, disrupting the flow. Bau et al. [2–5] studied DC MHD of saline solutions in microchannels made of ceramic tape. The microfluidic systems were mostly operated in an unsealed state due to gas bubble formation, but also to facilitate the introduction of fluids and flow visualization. It was also observed that the electrodes, made of gold paste, were consumed very quickly by electrolysis. Redox-based MHD pumping was

* Corresponding author. Present address: Tyndall National Institute, Life Science Interface Group, Lee Maltings, Prospect Row, Cork, Ireland. Tel.: +353 21 490 4075; fax: +353 21 427 0271.
E-mail address: alexandra.homsy@unine.ch (A. Homsy).
[1] Present address: Johannes Kepler University Linz, Institute for Microelectronics, Al-tenberger Strasse 69, A-4040 Linz, Austria.

Table 1
Performance comparison of previously published MHD pumps with our MHD pump

Ref.	U (V)	I (mA)	A (mm^2)	A_J (mm^2)	l (mm)	J (A m^{-2})	B (T)	ΔP_{MHD} (Pa)	υ_{MHD} (mm s^{-1})	Q_{MHD} (μL min^{-1})
[1]	30 DC	1.8	0.4	30	30	60	0.44	1	2.6*	63*
[6]	>1.3 DC	35	18	225	75	155	1.35	16	0.4	450×10^3
[2]	4 DC	15	1.9	292	172	51	0.4	3.5	0.4	45
[8]	6.6 AC	140	0.2	1.5	4	92105	0.013	5	1.5	18
[9]	5 AC	90	0.2	5	28	17684	0.011	5.5	0.24	3
[10]	4 AC	40	6×10^{-3}	2	63	21100	0.1	133	0.04	14×10^{-3}
[15]	16 DC	4.8	9×10^{-3}	1.2	16	4000	0.42	27	0.5	0.3
Here	19 DC	2	9×10^{-3}	1.2	16	1600	7.05	180	2.8	1.5

All values for voltage (U), current (I), channels' cross-sectional area (A), total length of electrodes along the pumping channel (l), MHD flow mean velocity in the pumping channel (υ_{MHD}) and MHD flow rate (Q_{MHD}) were experimental data, and were taken from Refs. [1,2,6,8–10]. Most of the values for the electrodes cross-sectional area (A_J) and current density (J) across the pumping channel had to be calculated. The body force (ΔP_{MHD}) generated by the pumps was calculated from Eq. (2).

* Both values were taken from experimental measurements. If calculated with relation (3), the predicted velocity and flow rate would be 0.16 mm s^{-1} and 4 μL min^{-1}, respectively.

studied by Leventis and Gao [6] and more recently by Clark and coworkers [7]. Other groups studied MHD pumping of saline solutions with combined AC magnetic fields and an AC current at high frequencies (≥1 kHz) to avoid bubble formation at the electrodes [8–11]. MHD pumping in the AC mode leads to low flow rates as a result of the low intensity of the AC magnets. This is because the operation of electromagnets under high frequency and current conditions is limited by induction heating [10] and Eddy current formation [11]. Table 1 compares experimental conditions and main properties for a consistent sample of MHD micropumps published so far. The compared micropumps had channel depths of 3 mm or less, and the pumped solutions were electrolytic solutions. The pumps that had the best performance in terms of flow rate and velocity were the ones with maximized current density (J), magnetic field intensity (B) and depth of channel (h), and this was achieved by maximizing the channels cross-sectional area (A). On the other hand, the best performance in terms of generated body force were the pumps with maximized J, B and electrode length (l), and this was achieved by minimizing the electrodes cross-sectional area (A_J). Applications for MHD pumping reported in the literature include the study of mixing [2,5,12], polymerase chain reaction (PCR) [9], separation methods [10,11], chaotic flow [13] and trace metals analysis [14].

With the help of an MHD pump that solves the bubble generation problem [15], we show in this paper MHD pumping for fluid delivery of high ionic strength solutions in a NMR magnet. In the bulky NMR magnet, we had to develop an alternative technique to allow accurate measurement of MHD flow rate. This method is compared with another measurement technique based on bead velocity. Examples of useful applications of MHD pumping combined with NMR detection are suggested in the conclusion.

2. Theory

The study of the interaction between a magnetic field (B) and moving, conducting fluids is called magnetohydrodynamics. When a DC ionic current density J is coupled to a perpendicular permanent B, a body force F_L (the "Lorentz" force) is generated in the other perpendicular direction (i.e. the direction of the microchannel) and will move electrolytic solutions in the microfluidic chip [10,16]:

$$\vec{F}_L = \vec{J} \times \vec{B} \cdot V_D \tag{1}$$

where V_D is the device volume (m^3). It is assumed that B is homogeneous, J is constant, that the bulk solution is electroneutral, and that the Hartmann number [3,17] is close to zero (poor conductivity of the medium, compared to metals or plasma fluids).

The flow along the length of the channel resulting from the Lorentz force has a flow profile similar to that of pressure-driven flow, and obeys Poiseuille law in microchannels [18]:

$$\Delta P = Q R_{hy} = \frac{F_L}{A} = JBl \tag{2}$$

where ΔP is the pressure drop in the channel (Pa), Q the volumetric flow rate (m^3 s^{-1}), R_{hy} the hydraulic resistance of the channel (N s m^{-5}), A the channel cross-section (m^2) and l is the length of the channel along which the current is applied (m). (Note that l generally does not equal L, the total length of the channel.) If no additional pressure gradient is imposed on the channel (e.g. by gravity), the flow rate induced by MHD in half-circular channels will follow the relation:

$$Q = \frac{3\pi}{128\mu} \frac{l}{L} h^4 JB \tag{3}$$

where μ is the absolute viscosity (Pa s) and h is the height of the channel (m). As Eq. (3) shows, the flow rate in the microchannel is proportional to the applied current density and magnetic flux density, as well as to the fourth power of the channel height.

3. Experimental methods

The principle of this MHD pump is to generate a high DC current density without disruption of flow due to bubble formation, and is described in Ref. [15]. Briefly, two micromachined frit-like structures connect the pumping channel to adjacent side

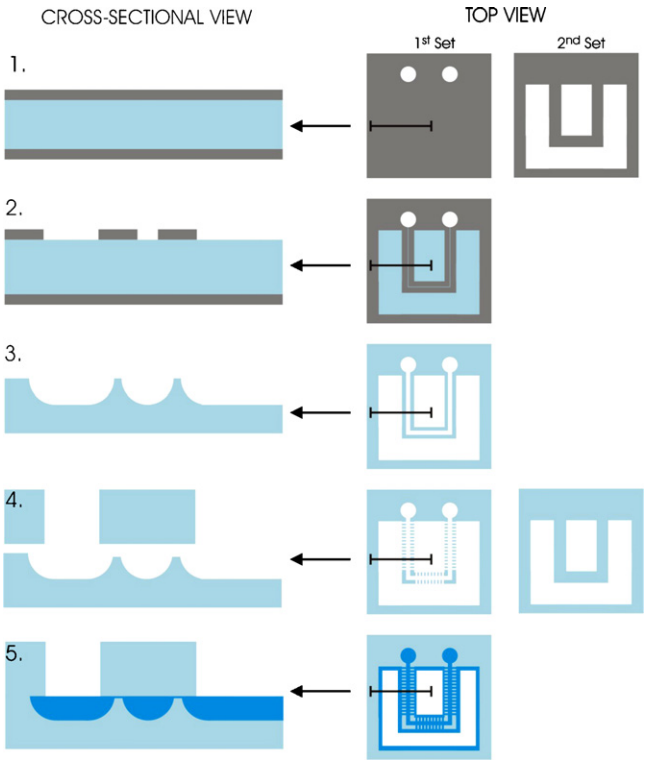

Fig. 1. Microfabrication steps for the micropump. (1) Start with Pyrex wafers coated with 400 nm CVD polysilicon. (2) Photolithography followed by RIE etching of polysilicon to define the channel and the side reservoirs location. (3) Deep etch in 20% HF: defines the length of the side channels. Polysilicon removal with KOH. (4) Photolithography with spray photoresist followed by BHF etch to form the shallow side channels; alignment of the wafer with a Pyrex coverplate. (5) Fusion bonding of both Pyrex wafers at 650 °C.

reservoirs. The electrodes are actually located in these side reservoirs, and are thus physically separated from the main channel in which flow is generated. In this way, bubbles formed at the electrodes never enter the main channel, escaping instead through open reservoirs to the atmosphere. A high ionic current with a very low volumetric flow rate can be generated over the main channel across the frit-like structures (these will be referred to as side channels from now on). When this ionic current is coupled to a perpendicular magnetic field, a body force is generated in the perpendicular direction, all along the pumping channel.

3.1. Micropump fabrication

We processed two complementary sets of Pyrex wafers in our cleanroom facility according to Ref. [15]. The first set of wafers includes the microchannel, and the second the holes for fluidic access to the side reservoirs. The design and fabrication process for the two sets of wafers are shown in Fig. 1. Before step 1, we dipped both sets[2] in 50% HF for 25 min. The result was through holes: 700 μm diameter holes in the first set for bottom access to the microchannel, and rectangular shaped holes in the second set for fluidic access from the top to the side reservoirs.

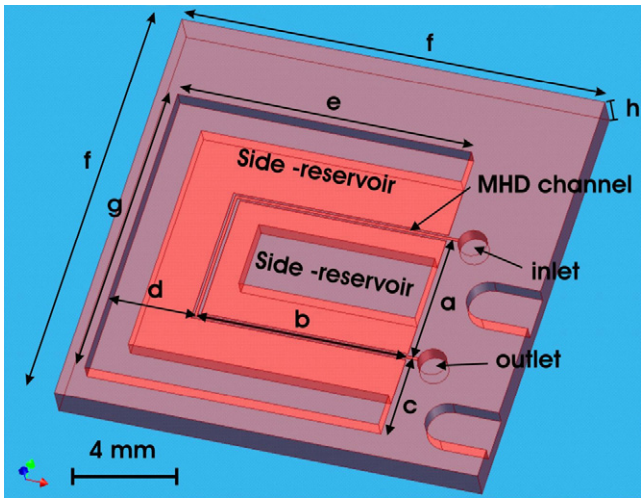

Fig. 2. Three dimensional drawing of the MHD pump (drawing courtesy of F. Lucklum). The dimensions of the chip and side reservoirs were: $a = 4$ mm, $b = 6$ mm, $c = 2.45$ mm, $d = 2.4$ mm, $e = 8.4$ mm, $f = 12.65$ mm, $g = 8.95$ mm, $h = 1$ mm. We measured the dimensions on a processed chip, with a precision of ± 0.05 mm.

The main channel (17 mm × 150 μm × 75 μm) is now U-shaped to make the overall dimensions of the pump smaller. A total number of 785 side channel were etched across the main channel. The side channels widths and spacing were 10 μm, the depth 100 nm and their length varied from 10 to 100 μm. The side reservoirs were 75 μm deep and their detailed dimensions are shown in Fig. 2. We initially planned a final step with evaporation of platinum electrodes on the bottom of the side reservoirs. However, this step was temporarily overlooked due to two technology problems related to electrical contact[3] and fusion bonding efficiency. Instead we incorporated platinum wire electrodes in the chip holder.

For pump encapsulation and fluidic connection with the outside, good care was taken in the choice of non-ferromagnetic material. In other words, the materials should not interact with the strong magnetic field of the NMR superconductive magnet. PMMA was chosen for the encapsulation of the pump. Fig. 3 shows a picture of the holder. O-rings were used for the fluidic sealing at the bottom chip-holder interface. The top cover of the holder was screwed on top of the chip. The screws were made in copper. This top cover had integrated platinum electrodes in fluidic contact with the side reservoirs of the chip. The sealing between the chip and the top cover was achieved using a thin sheet of latex. The sheet of latex was manufactured by pouring first a monolayer of liquid latex (XUR® liquid latex, Michael Schermons, Berlin, Germany) on a flat surface, letting it dry and then cutting a piece having the shape of the parts to seal together. The top cover played also the role of reservoir for ionic current generation. We connected the holder with outside capillaries with 062 Minstac fittings (The Lee Company, Westbrook, CT, USA).

[2] With structured 400 nm polysilicon and 1.8 μm of AZ1518 photoresist as an etch mask.

[3] The metal lines were disrupted at the edge of the channel, where the channel side-wall is nearly vertical.

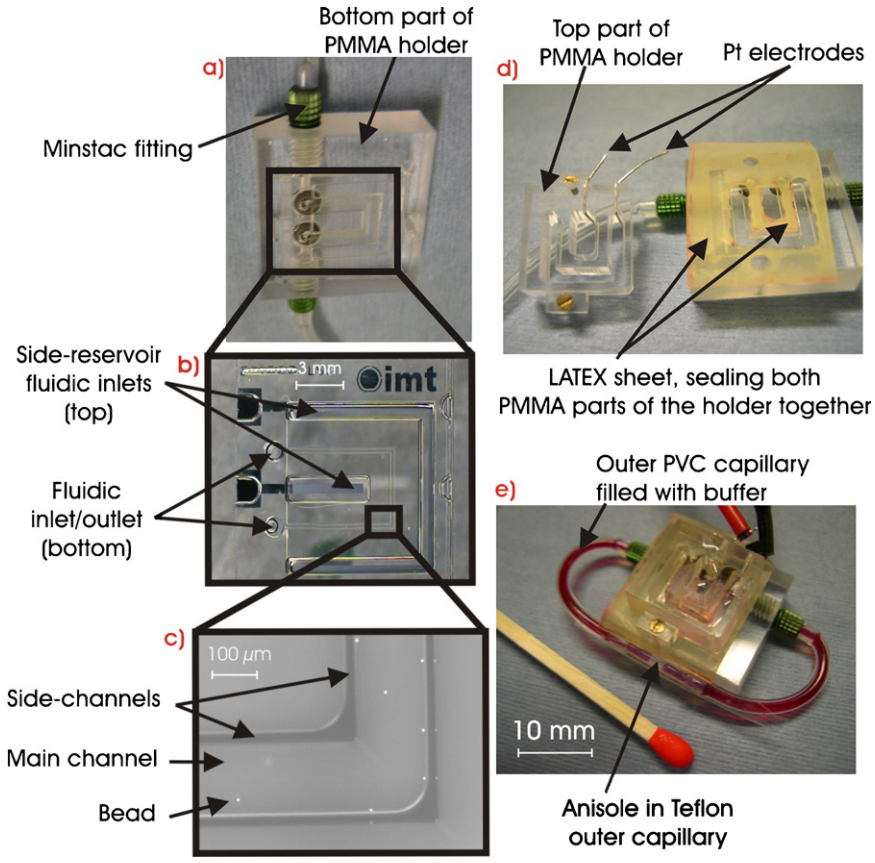

Fig. 3. (a) View of the chip on top of the O-rings on holder. (b) View of the chip with integrated platinum electrodes on the bottom of the side reservoirs. (c) Close-up view of a channel with flowing beads inside. (d) View of the chip with the latex sealing before closing the holder. (e) View of the encapsulated chip filled with amaranth-colored buffer. The anisole bubble is the transparent plug in between buffer seen on the outer capillary in front of the holder.

3.2. *Experimental setup*

The buffers composition were 53 mM citrate (pH 6), with 207 mM phosphate for 0.25 M buffer, and buffer supplemented with 244 mM or 744 mM KCl to reach ionic strengths of 0.5 M or 1 M, respectively. For each buffer concentration, we measured the pH and conductivity with electrodes from ThermoOrion company (Beverly, MA, USA). We saturated the buffer with amaranth, a red-colored salt, to bring visual contrast for flow observations. Conductivity measurements (see Table 2) showed that the addition of amaranth to the buffer did not bring significant changes to the electric properties of the buffer (i.e. <1% in conductivity). Polystyrene beads (carboxylate-modified microspheres, 2.55% in water, from Poly-sciences Europe GmbH, Germany) with a diameter of 6 μm were diluted 500 times in the buffer for flow visualization. A constant current (0–5 mA) was applied across the two Pt electrodes with a 2400 source meter from Keithley Instruments S.A. (Zurich, Switzerland), the compliance of the source was set to 100 V.

Table 2
Electric and chemical properties of the buffers [24]

	Conductivity (mS cm^{-1})	Resistivity (Ω m)	pH
0.25 M Buffer	21.4	0.47	6.3
0.5 M Buffer	44.9	0.22	6.0
1 M Buffer	88.3	0.11	5.8
1 M Buffer + Amaranth	87.8	0.11	5.9

We utilized NdFeB rare earth magnets (Forcefield, CO, USA) of varied magnetic field strength for the pumping experiments on top of permanent magnets. We chose magnet diameters of 50 mm (a diameter larger than the chip dimensions, see Fig. 4) and designed the chip holder as thin as possible to ensure good homogeneity of the magnetic field in the microchannel. The magnetic field intensities were measured with a 3-axis magnetic-field transducer (model 3MR-1C, Sentron AG, Switzerland). For those measurements, we positioned the Hall sensor at the exact height corresponding to the microchannel position. Therefore, we measured two different magnetic field intensities of $B_1 = 0.33$ and $B_2 = 0.38$ T. We performed the experiments within the NMR superconductive magnet in collaboration with Klaus Ehrmann of the LMIS3 laboratory in EPFL. This magnet was part of a 300 MHz NMR spectrometer setup (DRX 300, Bruker Biospin AG, Switzerland). The exact value for the resonance frequency of this magnet was measured in the laboratory: it is 300.1317 MHz. Combined with the scale factor (given by the magnet manufacturer) of 42.6 MHz T^{-1}, the intensity of the NMR magnet can be calculated to be 7.045 T. The working space inside this magnet was limited: it has a cylinder volume

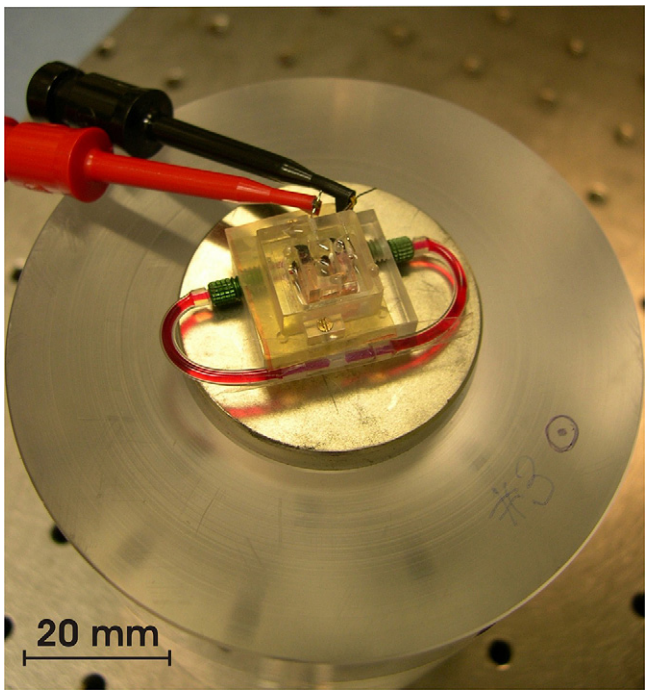

Fig. 4. View of the chip holder for measurement on top of a 40 mm diameter NdFeB permanent magnet (with 1.5 cm long Teflon flow measurement capillary).

of 40 mm diameter, and experiments had to be conducted at a specific height position where the field is uniform.[4] To fulfil these conditions, we designed a custom holder for the experiments inside the NMR magnet to allow the MHD pump to be positioned in the homogeneous field region, and to contact the Pt electrodes with the current source, located outside of the NMR instrument (see Fig. 5).

3.3. Flow measurement methods

We conducted the flow measurements in a closed loop fashion by connecting the inlet and the outlet of the PMMA holder with an off-chip PVC capillary (inner diameter of 1 mm). We measured the flow velocity with the same bead technique as described in Ref. [15]. Briefly, the linear flow velocity was determined by measuring the time required for beads to travel between two defined points in the pumping channel. Only beads having a maximum velocity (i.e. beads located in the middle of the channel) were considered.

In the 7 T magnet, we developed an indirect measurement method to observe MHD flow rate, as optical characterization was not possible in such an apparatus. We measured the lateral displacement of the interface of an anisole-bubble (2 mm long, 2 μL volume) trapped within the amaranth-colored buffer in a Teflon capillary (5 cm long, inner diameter of 0.81 mm) connected in between the outer PVC capillaries. We chose anisole for its immiscible properties with water, and because it has the same viscosity and density as water (see Table 3). However, the surface tension of anisole differed significantly from aqueous solutions, and the static contact angle of anisole with Teflon was measured to be 30°. Anisole wetted the Teflon wall of the capillary better than water. The whole surface of the Teflon tube was wetted back and forth by the anisole plug in between the buffer several times before actually performing each measurement. Hence hysteresis due to changes in the Teflon contact angle with the different liquids could be avoided. The initial position of the anisole bubble boundaries were physically marked on the tube, and a precise ruler with half millimeter scale was used to measure the displacement of the plug with respect to its initial position.

[4] This distance was approximately $h = 270$ mm from the bottom entrance of the NMR cylinder.

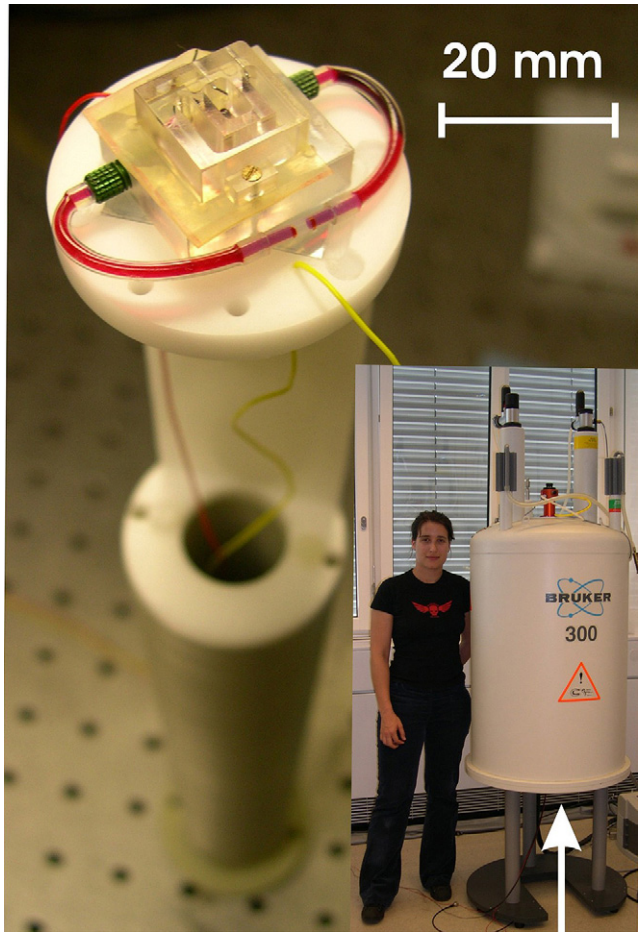

Fig. 5. View of the chip holder for measurement inside the bulky superconductive magnet (with 1.5 cm long Teflon flow measurement capillary). A picture of the NMR superconductive magnet is seen on the right. The holder is inserted into the NMR magnet from the bottom, as indicated by the white arrow.

Table 3
Physical properties of anisole and aqueous solutions at 20 °C

	Viscosity ($mPa\,s^{-1}$)	Relative density	Solubility in water	Surface tension ($nN\,m^{-1}$)
Anisole	1.06	0.99	Poor	35.1
Water	0.89	1	High	71.99
1 M Buffer	1.09	1	High	≤71.99

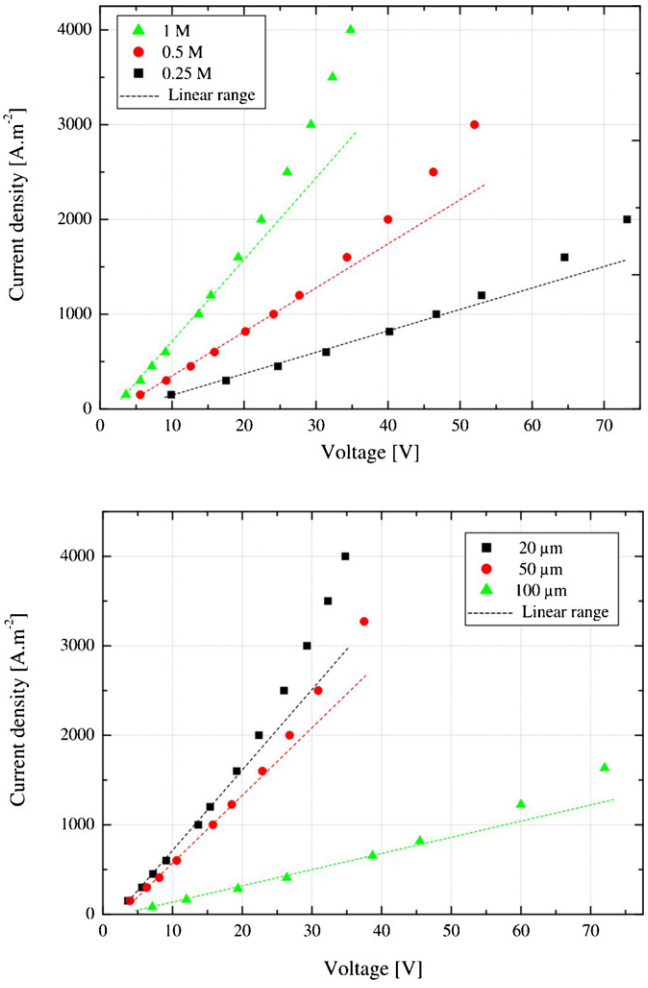

Fig. 6. Characterization of the chip with current–voltage curves. The deviation on the voltage measurement corresponds to 1% of each data value. The linear fit of the data is represented by the dotted lines. [Top] Chip behavior as a function of the ionic strength of the buffer (chip with 20 µm long side channels). [Bottom] Chip behavior as a function of the length of the side channels (chip filled with 1 M buffer).

4. Results and discussion

Fig. 4 shows a close-up top view of the encapsulated chip. The top reservoirs are filled with the buffer. When both side reservoirs and the main channel of the chip are filled, the ionic current can be generated between the electrodes. No electrode corrosion was observed at anytime on the platinum wires surface. We did not observe any flow in our system when only current or magnetic field was applied.

4.1. Electrical characterization

We first characterized the current–voltage behavior of the chip as a function of the conductivity of the solutions and the geometry of the side channels.

4.1.1. Ionic strength

The upper panel of Fig. 6 shows the current–voltage behavior for a micropump with 20 µm long side channels, filled with buffers of selected conductivities. We see that the higher the concentration, the higher the current for a fixed voltage. The current is rising linearly with the voltage until a certain point where the linearity is lost. Above this threshold, the temperature of the solution begins to rise: Joule heating becomes significant. The voltage threshold is different for each solution, it is higher for the less concentrated buffers.

4.1.2. Side channels length

When a given voltage is applied across the side channels, the electrical resistance of the pump will depend on the dimensions of the side channels. We developed an electrical model of the pump (see Fig. 7), and found that more than 95% of the voltage drop took place at the side channels. These features have thus a major influence on the electrical properties of the pump. More specifically, the longer the side channels, the higher the electrical resistance and therefore the less the current intensity in the main channel. We designed the new pump with four different side channel lengths, namely 10, 20, 50 and 100 µm. The aim of the side channels is to produce a DC ionic current as high as possible in the main channel for a given DC voltage without Joule heating in the main channel. The 100 nm deep side channels also separate the main channel from the reservoirs with Pt electrodes and prevent air bubbles from entering the main channel, and interfering with the operation of the pump. The bottom panel of Fig. 6 shows the current–voltage behavior of micropumps with

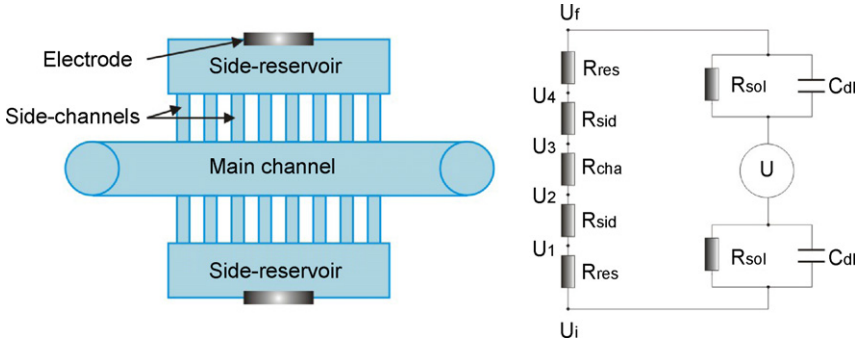

Fig. 7. Schematic top view of the pump and equivalent electrical scheme. Each channel geometry have a different electrical resistance: R_{res} is the resistance of the side reservoir area, R_{cha} the resistance of the main channel and R_{sid} is the resistance of all side channels in parallel in between one side reservoir and the main channel. The electrical resistance of the buffer R_{sol} in parallel with the capacitance C_{dl} represents the electrodes. C_{dl}, the double layer capacitance, stand for the polarization of the electrodes at the electrode–electrolyte interface.

Table 4
Comparison of the Joule heating thresholds as a function of: (1) the side channel lengths with 1 M buffer solution in the pumps; (2) the buffer ionic strengths in a pump with 20 μm long side channels

(1)	U (V)	J_{max} (A m^{-2})	Q_{diss} (W m^{-1})	Power (mW)	(2)	U (V)	J_{max} (A m^{-2})	Q_{diss} (W m^{-1})	Power (mW)
20 μm	19	1600	2.1	37	0.25 M	47	1000	3.4	57
50 μm	23	1600	2.6	45	0.5 M	28	1200	2.4	41
100 μm	45	818	2.7	45	1 M	19	1600	2.1	37

three different side channel lengths for a buffer solution of 1 M ionic strength. We see that, for the same buffer conductivity, the shorter the side channel length, the higher the current for a given voltage. The voltage threshold of the linear range is also different for each geometry. The voltage threshold is higher for the longest side channels geometries. Although the chips with the best bonding reproducibility were the 100 μm long channels, we conducted the experiments with MHD pumps of 20 and 50 μm side channels geometry. The current generated by the 100 μm long side channels was too small to achieve any noticeable MHD pumping with the permanent magnets. We also could not test MHD pumps with 10 μm long side channels as none of them bonded properly after the fusion bonding microfabrication step, because the available surface was too small to allow sufficient adhesion for fusion bonding.

4.1.3. Joule heating and power consumption

In Fig. 6 the Joule heating threshold has been determined for all three side channel lengths (20, 50 and 100 μm) with a 1 M buffer, as well as for all three buffer concentrations (0.25, 0.5 and 1 M) in a pump with 20 μm long side channels. Table 4 summarizes those values. The threshold for Joule heating occurs when the voltage–current behavior of the pump ceases to be linear. At this point, the system begins to heat up, and the increase in temperature changes the physical behavior of the pumped fluid [19]. For each of these thresholds, we also calculated the corresponding power dissipation Q_{diss} [15]:

$$Q_{diss} = \frac{(U-2)I}{l_{cap}} \tag{4}$$

where U is the voltage applied across the system (V), I the current (A) across the side channels and l_{cap} is the total length of the side channels[5] (m). Corresponding Q_{diss} vary from 2.1 to 3.4 W m^{-1}. The applied voltage should therefore not be higher than 19 V for MHD pumping of a 1 M solution with the 20 μm long side channel geometry, and 23 V for 1 M solution with 50 μm long side channels. Compared to other MHD micropumps, the power consumption of our pump is very low, and varies from 38 to 57 mW.

4.1.4. Bubble generation at electrodes

Another limiting factor that may affect our system in terms of duration of a single experiment is the rate of bubble generation around the Pt electrodes. We observed that after a certain time (30–60 min), the bubbles around the electrodes in the outer reservoir (on top of the holder) no longer escape in the air, but tend to stay in the space between the electrode, the PMMA reservoir and the buffer solution. This insulating gaseous spacing between the electrode and the buffer gradually decreases current generation between the electrodes (for a fixed voltage). This is so far the only time-limiting factor encountered with our pumping system, and it can be avoided by decreasing the operating current density (reducing the flow rate of the pump). This time limitation prevented us from performing flow rate measurements at high current density (>500 A m^{-2}) for durations longer than 30 min.

4.2. Characterization of the flow rate measurement method based on the anisole bubble

Inside the superconductive magnet, the flow rate was characterized by tracking the displacement of a liquid–liquid interface within a teflon capillary connected in a closed-loop fashion with the pump. The flow rate in the whole microfluidic system (Q) is directly proportional to the lateral displacement (dx) of the plug. For a given measurement time dt we will have:

$$Q = \frac{\mathrm{d}x}{\mathrm{d}t}\pi r_{CAP}^2 \tag{5}$$

where r_{CAP} is the radius of the teflon capillary used for the flow rate measurement. The continuity of the system implies that the flow rate is the same in the measuring capillary as it is in the microchannel (only the velocities differ). We used Eq. (3) for comparison with theory. We estimated the error on the displacement measurement to be half of the smallest graduation of our scale meter; the error was thus 0.25 mm.

Various interfaces were tested, the most reproducible results could be achieved by introducing a "bubble" of Anisole in the buffer solution. Anisole is a derivative of benzene, with similar viscosity and density as water. We conducted the flow rate measurements as follows. First the anisole plug was introduced in between the colored buffer in the teflon external capillary. A state of equilibrium was achieved when no movement of the plug was noticed. This equilibrium was reached after a mean waiting time of 30 min. Then the chip was fixed on top of the NMR chip holder (see Fig. 5) and inserted inside the NMR magnet. The measurement time began and ended when the current source was switched on and off, respectively. The plug position was recorded immediately after the current was switched off and the holder removed from the NMR magnet. As seen in the top

[5] This value is the sum of the lengths (10 μm) of all the 785 side channels located on both sides of the main channel.

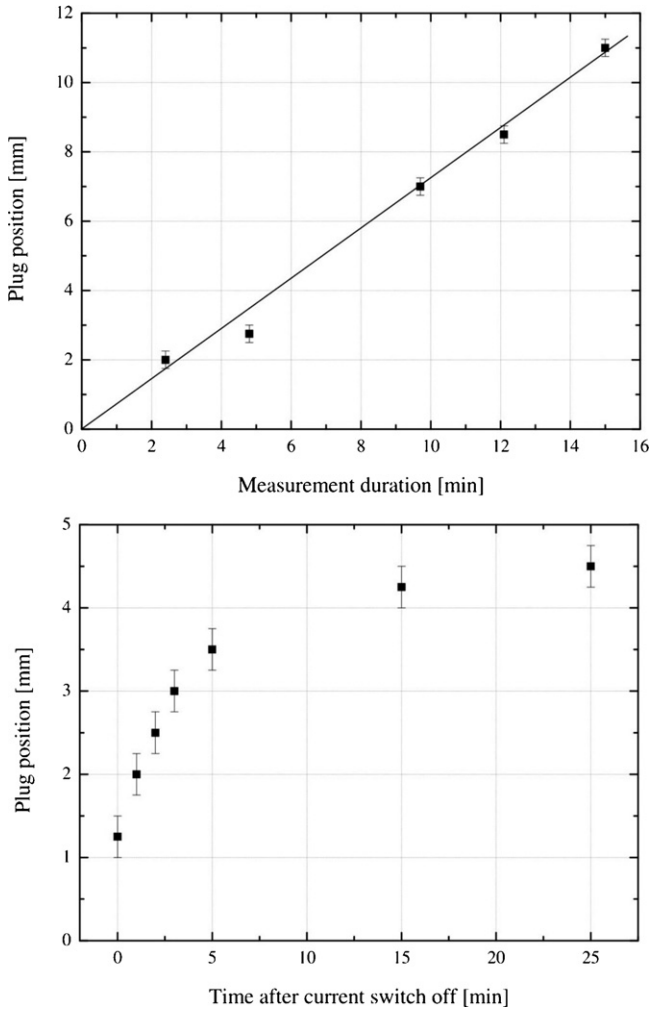

Fig. 8. Evolution of the plug position. [Top] As a function of the total measurement time (20 μm long side channels, 1 M Buffer, $J = 450\ \mathrm{A\,m^{-2}}$, $U = 6$ V, 5 cm long Teflon capillary). [Bottom] As a function of the waiting time after the end of measurement (50 μm long side channels, 1 M Buffer, $J = 610\ \mathrm{A\,m^{-2}}$, $U = 10$ V, 1.5 cm long Teflon capillary).

panel of Fig. 8, the plug's displacement is a linear function of the measurement time, as expected by the theory.

4.2.1. Backflow

The time gap between the current switch-off and the plug position measurement was less than 5 s. This remark is important because we noticed a movement of the plug in the direction opposite to MHD pumping after each measurement. This reverse movement usually did not exceed 10% of the total measurement for long Teflon measurement capillaries of typically 5 cm long. But in the case of a short measurement capillary (1.5 cm long, as depicted in Fig. 5) it could exceed 50%. This high reverse flow was measured for the 1.5 cm long capillary as a function of the elapsed time after measurement, and its evolution is seen in the bottom panel of Fig. 8. We see that the backflow is very fast within the first 5 min, and that it levels off after a waiting time of 15 min. This displacement in the reverse direction was also recorded 15 min after each measurement. We do not have a simple explanation for this phenomenon, but it is believed to be related to the interaction of anisole[6] and buffer with the Teflon capillary surface. For the rest of this work, we focused on system with 5 cm long teflon capillaries and avoided the backflow problem.

4.2.2. Equivalence with bead measurement technique

In order to validate the flow measurement technique based on the anisole bubble, we compared the ratios Q_x/B_x (at a given current density) with an existing technique based on the microscopic observation of the displacement of beads in the pump. Theory says that Q_x/B_x should be constant when J is constant. For $J = 650\ \mathrm{A\,m^{-2}}$, we had the following observations:

$$\frac{Q_{B_1}}{B_1} = 8.48 \times 10^{-2}\ \mu\mathrm{L\,min^{-1}\,T^{-1}},$$

$$\frac{Q_{B_2}}{B_2} = 8.42 \times 10^{-2}\ \mu\mathrm{L\,min^{-1}\,T^{-1}} \tag{6}$$

and

$$\frac{Q_{B_0}}{B_0} = 8.58 \times 10^{-2}\ \mu\mathrm{L\,min^{-1}\,T^{-1}} \tag{7}$$

where Q_{B_1} and Q_{B_2} were flow rates measured with the bead velocity technique and permanent magnets B_1 and B_2, and Q_{B_0} was the flow rate measured with the liquid–liquid interface technique in the NMR magnet of magnetic field intensity B_0. We see that all three ratios gave the same value (within 2%), showing that both measurement techniques are comparable.

4.3. Measurements with permanent magnets

In small B environments, i.e. when the MHD pump was characterized with permanent magnets, the flow rate was measured by means of bead velocity and anisole-bubble displacement. We did our measurements with MHD pumps having 20 μm long side channels, and 1 M buffer as the pumped solution. The maximum flow rates, corresponding to an applied current density of $650\ \mathrm{A\,m^{-2}}$, were respectively 0.028 and 0.032 $\mu\mathrm{L\,min^{-1}}$ for magnetic field intensities of $B_1 = 0.33$ T and $B_2 = 0.38$ T, respectively. The bead velocity as a function of the applied current density for two different permanent magnets can be seen in Fig. 9. We see that the measured flow is proportional to the applied current and that it follows theory.

This measurement was only possible if the fluidic system was closed by connecting the inlet and outlet with outside capillaries in a closed-loop fashion. In fact, the flow rate generated by MHD in small B environments seemed to be too weak to dispense any movement in an open system. This closed-loop fashion enabled us to get rid of the unnecessary backpressure due to hydrostatic and capillary forces. To understand the influence of hydrostatic pressure on the performance of the pump, we calculate the maximum body force generated by our pump. For a current density of $650\ \mathrm{A\,m^{-2}}$ and a permanent magnetic field of 0.38 T we have

[6] The presence of anisole even proved to slow down our flow rate measurements in some cases (as observed in the past paragraph of Section 4.3).

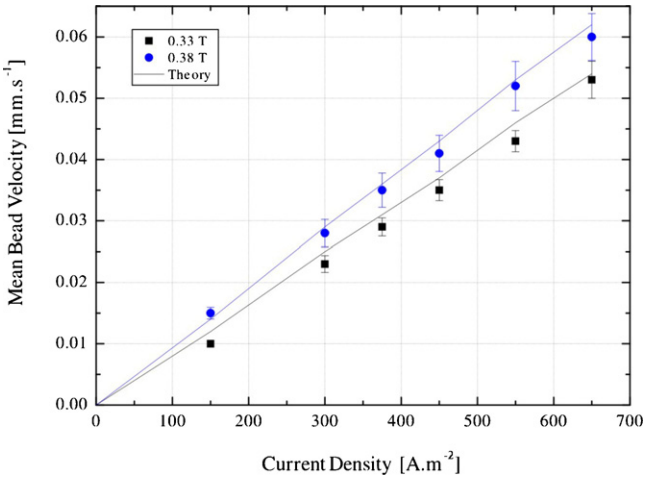

Fig. 9. MHD flow mean velocity as a function of current density (for two different magnetic field intensities, 20 μm long side channels and without anisole). The straight line is the theoretical mean velocity, calculated from Eq. (3).

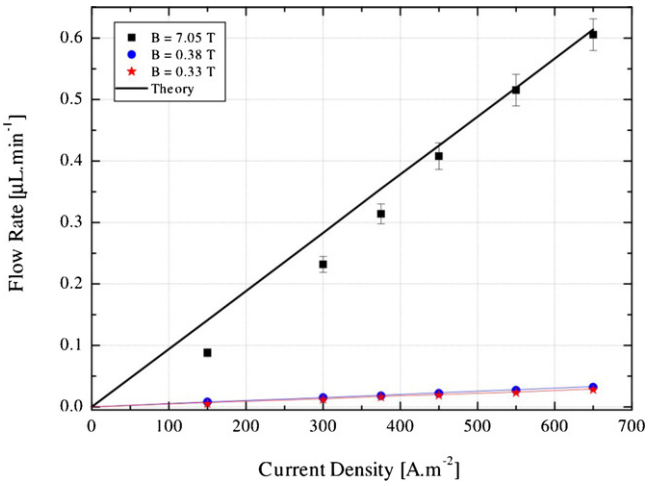

Fig. 10. MHD flow rate as a function of current density (for three different magnetic field intensities, and 20 μm long side channels). The straight line is the theoretical flow rate, calculated using Eq. (3).

(from Eq. (2)):

$$\Delta P = JBl = 650 \times 0.38 \times 16 \times 10^{-3} = 4\,\text{Pa} \tag{8}$$

This expression for the body force generated by our pump does not account for the influence of gravity. The hydrostatic pressure drop generated by gravity is proportional to the height difference (Δh) between two points so that:

$$\Delta P = \rho g \Delta h \tag{9}$$

where ρ is the fluid density and g ($\approx 9.8\,\text{m s}^{-2}$) is the gravity constant. If we calculate the threshold for Δh at which the hydrostatic pressure drop of our buffer equals the maximum MHD body force we obtain:

$$\Delta P = 4 = \rho g \Delta h \tag{10}$$

$$\Delta h = \frac{4}{10^3 \times 9.8} = 4.1 \times 10^{-4}\,\text{m} = 0.4\,\text{mm} \tag{11}$$

This means that if we try to measure the flow rate of our micropump by leaving the inlet and outlet open with a height difference higher than 0.4 mm (which is easily achievable) we will be unable to observe any movement induced by the MHD phenomenon only. The closed loop configuration of the system enabled us to cancel out the flow perturbation due to hydrostatic pressure.

Note that the bead flow measurements were not performed simultaneously with anisole bubble displacement. At low current densities (less than $500\,\text{A m}^{-2}$), the measured flow rates with the anisole interface technique were at least two times less than calculated from theory, and the less the current, the more the gap between theoretical flow rate and measurements. In fact the anisole bubble seemed to introduce a resistance to the flow for low current densities. This resistance was not observed when the beads only were present. Moreover, the equivalence of the two flow measurement methods with permanent magnets was only observed for high current densities (higher than $500\,\text{A m}^{-2}$). Therefore, we state that the bead measurement technique is a suitable technique for low flow rates measurements (5–30 nL min^{-1}), whereas the anisole bubble displacement is best for medium to high flow rates observations (30 nL min^{-1} to 1.5 μL min^{-1}). The useful range of these techniques overlap at medium flow rates, where we could carry out our comparison, and then validation of the anisole-based technique.

4.4. *Measurements in NMR superconductive magnet*

In the NMR environment, we characterized the flow with two different side channel lengths for the MHD pump geometry (namely 20 and 50 μm long) and 1 M buffer as the pumped solution. We measured the displacement of the anisole plug as a function of the applied current. In any case, we compared the measurements with theory. Every pump gave equivalent results, namely very good correspondences with theory. An example of the evolution of the flow rate in the NMR magnet as a function of current density for a pump with 20 μm long side channels is shown in Fig. 10. We see that the measured flow rate depends on the applied J and increases in a linear fashion, just like the flow with permanent magnet actuation. For low values of current, the measured flow rate is lower than our calculations, but corresponds again for $J \geq 450\,\text{A m}^{-2}$. This phenomenon at low J is believed to be related to capillary pressure issues. The results presented in Eqs. (6) and (7) can also be used to show that the volumetric flow rate scales with the magnetic field:

$$\frac{Q_{B_0}}{Q_{B_1}} = \frac{0.605}{0.028} = 21.6 \quad \text{and} \quad \frac{B_0}{B_1} = \frac{7.05}{0.33} = 21.4 \tag{12}$$

$$\frac{Q_{B_0}}{Q_{B_2}} = \frac{0.605}{0.032} = 18.9 \quad \text{and} \quad \frac{B_0}{B_2} = \frac{7.05}{0.38} = 18.5 \tag{13}$$

The change from the permanent magnets (B_1, B_2) to the NMR magnet (B_0) increased the field strength by a factor of 18.5 and 21.4, respectively. The MHD measurements (at a fixed current density of $650\,\text{A m}^{-2}$) showed an increase in the flow rate by a factor of 18.9 and 21.6, respectively. As the flow rates at a fixed current density for the same chip geometry are

directly proportional to the magnetic field strength (see Eq. (3)), the equivalence of the ratios proved the flow rate dependance on B.

The maximum body force generated by our pump for a current density of 1600 A m^{-2} and a NMR magnetic field of 7.05 T is:

$$\Delta P = JBl = 1600 \times 7.05 \times 16 \times 10^{-3} = 180.5\,\text{Pa} \quad (14)$$

which corresponds to a height difference (see Eq. (9)) of:

$$\Delta h = \frac{180.5}{10^3 \times 9.8} = 1.8 \times 10^{-2}\,\text{m} = 18\,\text{mm} \quad (15)$$

So far, the only MHD pump that generated a MHD body force of more than 100 Pa was fabricated by Eijkel et al. [10]. Combining an AC magnetic field of 0.1 T, an AC current density of 21100 A m^{-2}, on a total electrode length of 63 mm, they generated a maximum body force of 133 Pa.

To the regard of these results, we see that MHD pumping in an NMR environment has been successfully achieved. The MHD body force (180.5 Pa) and flow velocity (2.8 mm s^{-1}) performance in NMR environment of our pump surpassed any previously published MHD pumps of similar dimensions (see Table 1). The final aim of this work is to integrate our MHD pump together with planar coils in a microfluidic system for NMR analysis [20]. The high performance of the pump at relatively low flow rates is seen as an asset for NMR and MRI applications.

5. Conclusions

We developed a simple method of flow rate measurement inside the bulky NMR magnet, and we successfully achieved MHD pumping for the first time in an NMR environment in accordance with theory. The body force (180.5 Pa) and flow velocity (2.8 mm s^{-1}) performance in NMR environment of our pump surpassed any previously published MHD pumps of similar dimensions. The flow characterization method with immiscible fluids is suitable for high flow rate observation (namely for $J \geq 500$ A m^{-2}), whereas the bead velocity method is best for lower flow rate characterization on top of permanent magnets. Our future work with MHD pump should include the integration of NMR analysis microcoils to form a monolithic NMR microchip. In that regard, due to geometrical issues, the NMR coil to be integrated with our pump must generate the analyzing field in the direction of the plane of the chip, as in Ref. [21]. One envisioned application is the online monitoring of a fast kinetics chemical reaction with our pump also used as the mixer. Another interesting application for research in MHD profile analysis would be to visualize the flow generated by the micropump by on-chip Magnetic Resonance Imaging (MRI) techniques as in Refs. [22,23].

Acknowledgements

The devices were fabricated in the COMLAB, the joint cleanroom facility of IMT and CSEM, and we thank all the technical staff there for the helpful support. We also thank our project partner Klaus Ehrmann at EPFL (STI-IMM-LMIS3) for help in characterization of our pump in NMR environment. Thanks to Peter van der Wal for his relevant remarks and advice. This work was supported by an EPFL Presidential Fund (Nr. 581.552) and by the Swiss National Science Foundation (Project Nr. 2100-61549.00).

References

[1] J. Jang, S. Lee, Theoretical and experimental study of MHD magnetohydrodynamic micropump, Sens. Actuators A 80 (2000) 84–89.
[2] H. Bau, J. Zhong, M. Yi, A minute magnetohydrodynamic (MHD) mixer, Sens. Actuators B 79 (2001) 207–215.
[3] J. Zhong, M. Yi, H. Bau, Magneto hydrodynamic (MHD) pump fabricated with ceramic tapes, Sens. Actuators A 96 (2002) 59–66.
[4] H. Bau, J. Zhu, S. Qian, Y. Xiang, A magneto-hydrodynamically controlled fluidic network, Sens. Actuators B 88 (2003) 205–216.
[5] S. Qian, H. Bau, Magneto-hydrodynamic stirrer for stationary and moving fluids, Sens. Actuators B 106 (2005) 859–870.
[6] N. Leventis, X. Gao, Magnetohydrodynamic electrochemistry in the field of Nd–Fe–B magnets. Theory, experiment, and application in self-powered flow delivery systems, Anal. Chem. 73 (2001) 3981–3992.
[7] P. Arumugam, E. Clark, I. Fritsch, Use of paired, bonded NdFeB magnets in redox magnetohydrodynamics, Anal. Chem. 77 (2005) 1167–1171.
[8] A. Lemoff, A. Lee, An AC magnetohydrodynamic micropump, Sens. Actuators B 63 (2000) 178–185.
[9] J. West, B. Karamata, B. Lillis, J. Gleeson, J. Alderman, J. Collins, W. Lane, A. Mathewson, H. Berney, Application of magnetohydrodynamic actuation to continuous flow chemistry, Lab On a Chip 2 (2002) 224–230.
[10] J. Eijkel, C. Dalton, C. Hayden, J. Burt, A. Manz, A circular ac magnetohydrodynamic micropump for chromatographic applications, Sens. Actuators B 92 (2003) 215–221.
[11] J. Bao, D. Harrison, Fabrication of microchips for running liquid chomatography by magnetohydrodynamic flow, in: Seventh International Conference on Miniaturized Chemical and Biochemical Analysis Systems, Squaw Valley, California, USA, 2003, pp. 407–410.
[12] J. West, J. Gleeson, J. Alderman, J. Collins, H. Berney, Structuring laminar flows using annular magnetohydrodynamic actuation, Sens. Actuators B 96 (2003) 190–199.
[13] Y. Xiang, H. Bau, Complex magnetohydrodynamic low-reynolds-number flows, Phys. Rev. E 68 (2003) 016312.
[14] E. Clark, I. Fritsch, Anodic stripping voltametry enhancement by redox magnetohydrodynamics, Anal. Chem. 76 (2004) 2415–2418.
[15] A. Homsy, S. Koster, J. Eijkel, A. van den Berg, F. Lucklum, E. Verpoorte, N. de Rooij, A high current density DC magnetohydrodynamic (MHD) micropump, Lab On a Chip 5 (2005) 466–471.
[16] R. Feynman, R. Leighton, M. Sands, The Feynman Lectures on Physics, vol. II, Addison Wesley Longman, 1964.
[17] P. Davidson, An Introduction to MHD, Cambridge University Press, 2001.
[18] P. Gravesen, O. Jensen, J. Branebjerg, Microfluidics—a review, J. Micromech. Microeng. 3 (1993) 168–182.
[19] R. Nelson, A. Paulus, A. Cohen, A. Guttman, B. Karger, Use of Peltier thermoelectric devices to control column temperature in high-performance capillary electrophoresis, J. Chromatogr. 480 (1989) 111–127.
[20] C. Massin, F. Vincent, A. Homsy, K. Ehrmann, G. Boero, P.-A. Besse, A. Daridon, E. Verpoorte, N. de Rooij, R. Popovic, Planar microcoil-based microfluidic NMR probes, J. Magn. Reson. 164 (2003) 242–255.
[21] K. Minard, G. Holtom, L. Kathmann, P. Majors, B. Thrall, R. Wind, Simultaneous 1H PFG-NMR and confocal microscopy of monolayer cell cultures: Effects of apoptosis and necrosis on water diffusion and compartmentalization, Magn. Reson. Med. 52 (2004) 495–505.

[22] A. Goloshevsky, J. Walton, M. Shutov, J. de Ropp, S. Collins, M. McCarthy, Integration of biaxial planar gradient coils and an RF microcoil for NMR flow imaging, Meas. Sci. Technol. 16 (2005) 505–512.

[23] S. Ahola, F. Casanova, J. Perlo, K. Muennemann, B. Bluemich, S. Stapf, Monitoring of fluid motion in a micromixer by dynamic NMR microscopy, Lab On a Chip 6 (2006) 90–95.

[24] D. Lide, C.R.C. Handbook of Chemistry and Physics, 76th ed., CRC Press, 1995.

Biographies

A. Homsy obtained her master of science in physics engineering from the Swiss Federal School of Technology (EPFL), Switzerland, in 1999. For her PhD she went to the University of Neuchatel, Institute of Microtechnology, Switzerland, where she worked on the design of DC magnetohydrodynamic micropumps for NMR environment. Her current research focuses on microfluidic systems for protein microarrays with integrated photon detection.

Vincent Linder was born in 1975 and studied Chemistry at the University of Neuchâtel, Switzerland. He engaged in a PhD program in collaboration between the Microtechnology department of the University of Neuchâtel, the University Hospital of Berne and CSEM SA, and focused on the development of microfluidic chips for clinical assays. He continued his work on the development of microfluidic devices for applications in Life Sciences at Harvard University with Prof. Whitesides. Dr Linder is currently commercializing microfluidic devices for clinical applications, in a collaboration between Claros Diagnostics and Prof. de Rooij at the University of Neuchâtel.

Frieder Lucklum graduated at the Otto-von-Guericke University Magdeburg, Germany, in 2005, and received his Dipl.-Ing. (M.Sc.) degree in micro system technology from the Sensor and Micro Systems Group. Since 2006, he has been working as a university assistant in the Institute for Microelectronics at the Johannes Kepler University Linz, Austria, and researching on his Ph.D. thesis in the field of acoustic microsensors. His research activities include magnetoacoustic resonators, the basic physical mechanisms involved and their possible applications, as well as optimization of electromagnetic detectors.

Nicolaas F. de Rooij received his M.Sc. degree in physical chemistry from the State University of Utrecht, The Netherlands, in 1975, and a Ph.D. degree from Twente University of Technology, The Netherlands, in 1978. From 1978 to 1982, he worked at the Research and Development Department of Cordis Europa N.V., The Netherlands. In 1982, he joined the Institute of Microtechnology of the University of Neuchâtel, Switzerland (IMT UNI-NE), as professor and head of the Sensors, Actuators and Microsystems Laboratory. Since October 1990 till October 1996 and again from October 2002, he is acting as director of the IMT UNI-NE. He lectured at the Swiss Federal Institute of Technology, Zurich (ETHZ), and since 1989, he has been a part-time professor at the Swiss Federal Institute of Technology, Lausanne (EPFL). His research activities include microfabricated sensors, actuators, and microsystems. He was a member of the steering committee of the International Conference on Solid-State Sensors and Actuators and of Eurosensors. He acted as European Program Chairman of Transducers '87 and General Chairman of Transducers '89. He is a member of the editorial boards for the journals Sensors and Actuators, Sensors and Materials and the IEEE Journal of Microelectromechanical Systems. Dr. de Rooij is an IEEE Fellow.